ACS APPLIED MATERIALS & INTERFACES

Research Article

www.acsami.org

MnO_x Nanoparticle-Dispersed CeO_2 Nanocubes: A Remarkable Heteronanostructured System with Unusual Structural Characteristics and Superior Catalytic Performance

Sudarsanam Putla,[†] Mohamad Hassan Amin,[†] Benjaram M. Reddy,[‡] Ayman Nafady,[⊥,§] Khalid A. Al Farhan,[⊥] and Suresh K. Bhargava*[,†]

[†]Centre for Advanced Materials and Industrial Chemistry (CAMIC), School of Applied Sciences, RMIT University, Melbourne VIC 3001, Australia

[‡]Inorganic and Physical Chemistry Division, CSIR—Indian Institute of Chemical Technology, Uppal Road, Hyderabad 500 007, India

[⊥]Chemistry Department, College of Science, King Saud University, Riyadh, Saudi Arabia

[§]Chemistry Department, Faculty of Science, Sohag University, Sohag 82524, Egypt

Supporting Information

ABSTRACT: Understanding the interface-induced effects of heteronanostructured catalysts remains a significant challenge due to their structural complexity, but it is crucial for developing novel applied catalytic materials. This work reports a systematic characterization and catalytic evaluation of MnO_x nanoparticle-dispersed CeO_2 nanocubes for two important industrial applications, namely, diesel soot oxidation and continuous-flow benzylamine oxidation. The X-ray diffraction and Raman studies reveal an unusual lattice expansion in CeO_2 after the addition of MnO_x. This interesting observation is due to conversion of smaller sized Ce^{4+} (0.097 nm) to larger sized Ce^{3+} (0.114 nm) in cerium oxide led by the strong interaction between MnO_x and CeO_2 at their interface. Another striking observation noticed from transmission electron microscopy, high angle annular dark-field scanning transmission electron microscopy, and electron energy loss spectroscopy studies is that the MnO_x species are well-dispersed along the edges of the CeO_2 nanocubes. This remarkable decoration leads to an enhanced reducible nature of the cerium oxide at the MnO_x/CeO_2 interface. It was found that MnO_x/CeO_2 heteronanostructures efficiently catalyze soot oxidation at lower temperatures (50% soot conversion, T_{50} ~660 K) compared with that of bare CeO_2 nanocubes (T_{50} ~723 K). Importantly, the MnO_x/CeO_2 heteronanostructures exhibit a noticeable steady performance in the oxidation of benzylamine with a high selectivity of the dibenzylimine product (~94−98%) compared with that of CeO_2 nanocubes (~69−91%). The existence of a strong synergistic effect at the interface sites between the CeO_2 and MnO_x components is a key factor for outstanding catalytic efficiency of the MnO_x/CeO_2 heteronanostructures.

MnO_x/CeO_2 Hetero-nanostructures Show a Remarkable Catalytic Oxidation Performance due to Catalytically Favorable Properties at MnO_x/CeO_2 Interface

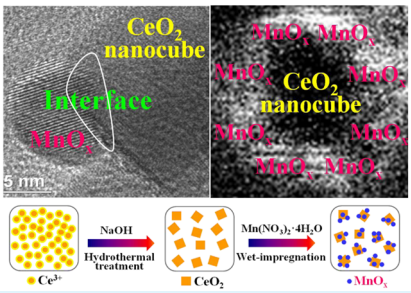

KEYWORDS: *heteronanostructures, cerium oxide, manganese oxide, characterization, interface effects, catalytic oxidation performance*

1. INTRODUCTION

Nanoscale heterostructures constituting various combinations of metals and/or metal oxides are promising materials in many fields, including catalysis.[1−5] They exhibit exceptional physicochemical and catalytic properties that are distinctly different from individual bulk components due to quantum-size, surface, and interface effects. The combination of nanosized cerium dioxide (CeO_2) with transition metal oxides, like manganese oxide (MnO_x), represents an interesting family of catalytic systems because of their economic, environmental, and catalytically favorable properties.[6−14] For example, both CeO_2 and MnO_x are abundant, cheap, and nontoxic candidates. They exhibit excellent redox properties and superior oxygen storage/release ability because of the multiple valences of Ce (III and IV) and Mn (II, III, IV, and VII). These attractive properties make the MnO_x/CeO_2 mixed oxides a viable alternative to precious metal-based catalysts (Au, Pd, and Pt) for many important catalytic applications, such as CO oxidation,[10] soot oxidation,[11] mercury oxidation,[12] formaldehyde oxidation,[13] and combustion of volatile organic compounds.[14] Therefore, significant research interest has been focused on modifying the unique properties of CeO_2 and MnO_x to ultimately enhance their catalytic performance.

Received: May 8, 2015
Accepted: July 13, 2015
Published: July 27, 2015

DOI: 10.1021/acsami.5b03988
ACS Appl. Mater. Interfaces 2015, 7, 16525−16535

The properties of heteronanostructures can be precisely tuned by varying their composition, size, shape, and morphology.[15] With the development of nanotechnology and nanoscience, considerable efforts have been made to develop CeO_2 nanomaterials with controlled morphologies and with preferentially exposed crystallographic planes that show enhanced redox and catalytic properties.[16−20] It has been reported that ceria nanocubes show a higher catalytic efficiency compared to that of polycrystalline ceria.[21−23] The main difference is that ceria nanocubes expose highly reactive (100) planes, whereas polycrystalline CeO_2 exposes the less reactive (111) facets. It has been demonstrated that the energy required for forming reactive oxygen vacancy defects on the (100) surface is much lower than on the (111) surface.[21−23] Consequently, CeO_2 nanocubes have been employed as effective catalysts and active supports in a number of catalytic applications. Conversely, the addition of MnO_x to CeO_2 nanocubes is expected to result in improved physicochemical properties, which are attributed to a cooperative effect between the Mn- and Ce-oxides at their heterostructured interface.[24−28] In particular, the high dispersion of MnO_x species on CeO_2 nanocubes leads to the formation of reactive interface active sites, which can eventually assist to achieve better results in catalytic reactions. Hence, in this study, MnO_x/CeO_2 heteronanostructures have been developed via synthesis of CeO_2 nanocubes using an alkaline hydrothermal method followed by dispersion of MnO_x (10 wt % of Mn with respect to Ce) onto the surface of CeO_2 nanocubes using a wet impregnation method. Uniformly sized CeO_2 cubes are formed with an average diameter of 20 ± 2 nm. The MnO_x species are found to be spherical in shape with an average diameter of 9 ± 1 nm.

In recent years, the fundamental understanding of interface chemistry between two domains has become a relevant field of study.[15,29] This interest, especially in catalysis, is due to the fact that two-phase interfaces could provide hybrid junctions with superior redox and catalytic properties. In addition, interfaces play a predominant role in the binding, transformation, and transport of surface species, such as electrons, adsorbents, and intermediates between two phases, which are beneficial for achieving better results in catalysis. Nanomaterials exhibit unusual properties compared with that of bulk materials. Hence, it is possible to find new insights when studying the nanointerface chemistry between two nanosized objects. However, understanding the interface-induced effects in heteronanostructures remains a significant challenge due to their structural complexity. This is crucial for developing novel applied catalytic materials. Therefore, in this work, special attention has been paid to understanding the characteristics of MnO_x/CeO_2 heteronanostructures at their interface and their role in catalysis. For this, a number of advanced characterization techniques, such as transmission electron microscopy (TEM), high resolution transmission electron microscopy (HRTEM), high angle annular dark-field scanning transmission electron microscopy (HAADF-STEM), electron energy loss spectroscopy in STEM mode (STEM-EELS), X-ray diffraction (XRD), N_2-adsorption−desorption analysis, X-ray photoelectron spectroscopy (XPS), and Raman spectroscopy have been employed in this study. Both CeO_2 and MnO_x are widely used oxides in catalytic oxidation reactions due to the existence of multiple oxidation states and superior redox properties.[6−14] Hence, the catalytic efficiency of the MnO_x/CeO_2 heteronanostructures was investigated for two important industrial catalytic applications: diesel soot oxidation and continuous-flow benzylamine oxidation. For comparison, the catalytic oxidation performance of pure CeO_2 nanocubes was also studied under identical conditions.

2. EXPERIMENTAL SECTION

2.1. Catalyst Preparation. The CeO_2 nanocubes were synthesized using a template-free alkaline hydrothermal method. In brief, the required quantity of $Ce(NO_3)_3{\cdot}6H_2O$ was dissolved in deionized water under stirring conditions. An aqueous 60 mL of NaOH solution (6 M) was added dropwise to the above solution, and the stirring was continued for 30 min at room temperature. The solution was then transferred to a Teflon bottle and sealed tightly in a stainless-steel autoclave. The hydrothermal treatment was performed at 453 K for 24 h. After cooling, the sample was collected, centrifuged several times with deionized water, and oven-dried at 373 K for 12 h. Finally, the sample was calcined at 773 K for 4 h in air with a heating ramp of 1 K/min.

The deposition of MnO_x (10 wt % of Mn with respect to Ce) on CeO_2 nanocubes was performed using a wet impregnation method. In a typical procedure, the desired quantity of $Mn(NO_3)_2{\cdot}4H_2O$ was dissolved in deionized water, followed by the addition of finely powdered CeO_2 nanocubes. The excess water was evaporated on a hot plate under mild stirring conditions at 373 K. The obtained sample was oven-dried at 373 K for 12 h and then calcined at 773 K for 4 h in air with a heating ramp of 1 K/min.

2.2. Catalyst Characterization. *2.2.1. Powder XRD Studies.* The powder XRD studies were conducted using a Rigaku diffractometer with Cu Kα radiation (1.540 Å) as the source. The diffractograms were recorded in the 2θ range of 10−80° with a 2θ step size of 0.02° and a step time of 2.4 s. The lattice parameter of the samples was estimated by a standard cubic indexation method using the intensity of the most prominent peak of CeO_2 (111). The average ceria crystallite size of the samples was estimated using a Scherrer equation.

2.2.2. Raman Analysis. Raman experiments were performed using a PerkinElmer-Raman Station 400F spectrometer equipped with a liquid N_2 cooled charge-coupled device detector and a confocal microscope. A 350 mW near-infrared 785 nm laser was used for analysis under ambient conditions. The wavenumber values reported from the spectra are accurate to within 2 cm^{-1}.

2.2.3. N_2 Adsorption−Desorption Studies. The BET surface area of the samples was determined by means of N_2 adsorption-desoprtion analysis at 77 K. A Micromeritics ASAP 2020 instrument was used for these studies. Prior to analysis, the sample was degassed under vacuum for 30 min at ambient temperature followed by fast-mode degassing at 423 K for 12 h. The BET surface area was calculated by utilizing the desorption data. Pore size and pore volume of the samples were estimated using the BJH method applied to the desorption leg of the isotherms.

2.2.4. XPS Studies. The XPS studies were performed using a Thermo K-alpha XPS instrument at a pressure $<10^{-7}$ Torr. The general scan and Ce 3d, Mn 2p, and O 1s core level spectra were recorded using Al Kα radiation (photon energy = 1486.6 eV) at a pass energy of 50 eV and electron take off angle (angle between electron emission direction and surface plane) of 90°. The core level binding energies (BEs) were charge corrected with respect to the carbon (C 1s) peak at 284.6 eV.

2.2.5. Transmission Electron Microscopy Studies. The TEM-HRTEM studies were carried out on a JEOL JEM-2100F instrument equipped with a slow-scan CCD camera, and the accelerating voltage of the electron beam was 80 kV. The preparation of samples for TEM-HRTEM analysis involved sonication in ethanol for 2−5 min followed by deposition of a few drops on a copper grid. The specimen was examined under vacuum at room temperature. STEM-EELS analysis was carried out using a JEM-2100F equipped with a Gatan Imaging Filter (GIF) operating at 80 kV. For STEM nanoanalysis, a tiny 0.5 nm diameter electron probe was used.

2.3. Activity Measurements. *2.3.1. Diesel Soot Oxidation.* The catalytic efficiency of the samples for diesel soot oxidation was

DOI: 10.1021/acsami.5b03988
ACS Appl. Mater. Interfaces 2015, 7, 16525−16535

conducted in a thermogravimetric analyzer (Mettler Toledo, TGA/SDTA851e). The experiments consisted of heating the catalyst−soot mixtures at a rate of 10 K/min from ambient temperature to 1273 K under a 100 mL/min flow of air. The activity measurements were performed under tight contact conditions with catalyst−soot mixtures in a 4:1 wt/wt ratio. The soot used in this study was Printex-U provided by Degussa. This soot was proven to be an appropriate model for the soot oxidation reaction. Each test was repeated three times to ensure the reproducibility of the obtained results; the maximum deviation from the mean value over the three tests was ±5 K. Temperatures corresponding to 50% soot conversion (denoted as T_{50}) were taken as indices of the activity of the tested catalysts.

2.3.2. Continuous-Flow Benzylamine Oxidation. The benzylamine oxidation was performed under vapor phase conditions (continuous-flow) using O_2 as the oxidant. In a typical experiment, 300 mg of sample was taken in a quartz microreactor (i.d. 0.8 cm) and placed vertically inside a tubular furnace. The catalyst was preheated at 473 K for 2 h before the catalytic runs. The benzylamine was fed with a motorized syringe pump into the vaporizer at a rate of 0.5 mL/h, and the O_2 was at a flow rate of 60 mL/min. To monitor the progress of the reaction under consideration, the condensed liquid products were collected at the bottom of the reactor and were confirmed by GC-MS equipped with a DB-5 capillary column and a flame ionization detector (FID). Samples were taken periodically during the reaction and analyzed by GC equipped with a BP-20 (wax) capillary column and an FID. The benzylamine conversion and products selectivity were calculated as per the procedure described elsewhere.

3. RESULTS AND DISCUSSION

3.1. Characterization Studies. Scheme 1 shows a typical procedure for the synthesis of MnO_x/CeO_2 heteronanostructures. The TEM-HRTEM studies have been carried out to elucidate the morphology of the Ce- and Mn-oxides as well as to estimate their particle size. The TEM picture of the as-synthesized CeO_2 shows the cubic morphology of CeO_2 (Supporting Information, Figure S1). Figure 1 shows HRTEM images of the CeO_2 cubes after calcination at 773 K. It was obvious that most of the CeO_2 cubes are uniform in size with an average diameter of 20 ± 2 nm. The lattice fringes of the CeO_2 cubes are clearly visible (Figure 1C and D). The estimated d spacing for the CeO_2 phase was found to be ∼0.27 nm, indicating that the CeO_2 cubes preferentially expose the (100) facets (Figure 1C and D and Supporting Information, Figure S1). The CeO_2 (100) surface is highly defective and contains a high concentration of oxygen vacancies compared to the (111) and (110) surfaces, which is beneficial from a catalytic point of view.[30−32] Conversely, the calculated particle size of the MnO_x species was ∼9 ± 1 nm (Figure 2). The interplanar spacing of fringes was found to be 0.166 and 0.236 nm, which corresponds to the spacing of the α-Mn_2O_3 (440) and α-MnO_2 (121) phases.[33,34] It is obvious from Figure 2 that the MnO_x species are present along the edges of the CeO_2 nanocubes. This interesting decoration may lead to highly reactive MnO_x/CeO_2 interfaces, which could play a favorable role in catalysis.

Figure 3A shows the powder XRD patterns of CeO_2 nanocubes and MnO_x/CeO_2 heteronanostructures. Several diffraction peaks are found at 2θ values of 28.26, 32.83, 47.25, 56.03, 69.2, 76.51, and 78.91°, indicating the presence of fluorite-structured cerium dioxide in the synthesized samples.[35,36] Additionally, two broad XRD peaks are found at ∼35.08 and 38.23° for the MnO_x/CeO_2 sample, which can be assigned to α-Mn_2O_3 phase.[37] Interestingly, the XRD peaks of the MnO_x/CeO_2 heteronanostructures are shifted considerably to lower angles compared with those of pure CeO_2 cubes (inset of Figure 3A). For this unusual behavior to be understood, the lattice parameters of the samples are estimated (Table 1).[38] The MnO_x/CeO_2 sample shows a higher lattice parameter compared with that of pure CeO_2. The radii of Mn ions (Mn^{2+} = 0.083 nm, Mn^{3+} = 0.065 nm, and Mn^{4+} = 0.053 nm) are

Scheme 1. Schematic Process for the Synthesis of MnO_x/CeO_2 Heteronanostructures

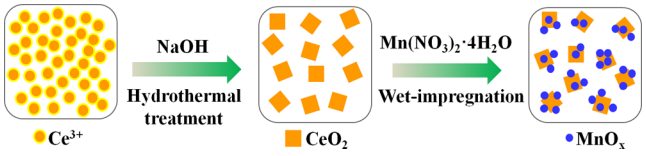

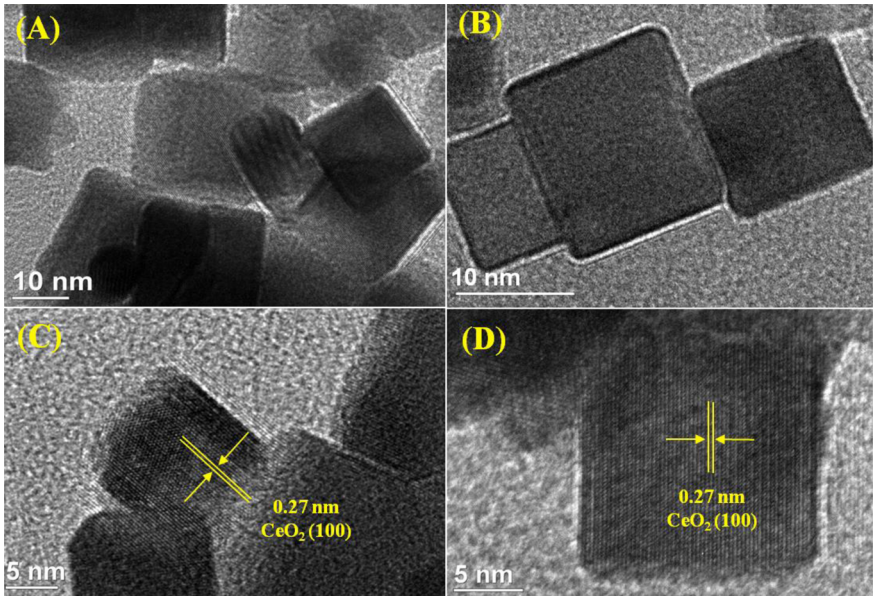

Figure 1. HRTEM images of the CeO_2 nanocubes after calcination at 773 K at different magnifications.

DOI: 10.1021/acsami.5b03988
ACS Appl. Mater. Interfaces 2015, 7, 16525−16535

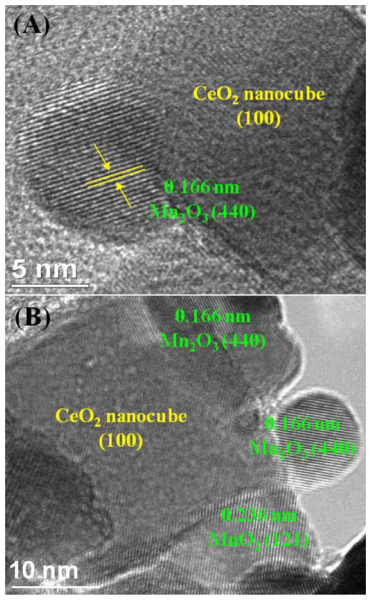

Figure 2. HRTEM images of the MnO_x/CeO_2 heteronanostructures with different magnifications.

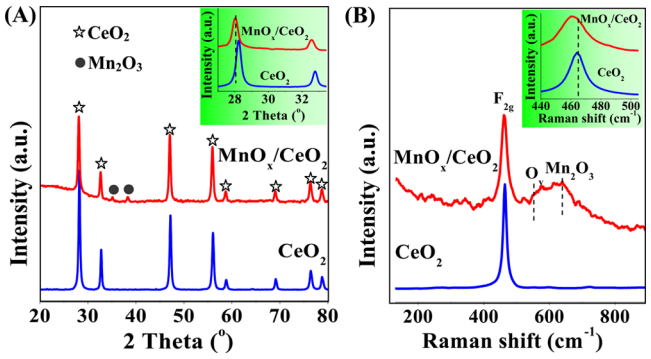

Figure 3. (A) Powder XRD patterns and (B) Raman spectra of the CeO_2 and MnO_x/CeO_2 samples.

Table 1. CeO_2 Crystallite Size (D), BET Surface Area (S_{BET}), Pore Size (P), Pore Volume (V), and CeO_2 Lattice Parameter (LP) of the CeO_2 and MnO_x/CeO_2 Samples

sample	D (nm)[a]	S_{BET} ($m^2\ g^{-1}$)	P (nm)[b]	V ($cm^3\ g^{-1}$)[b]	LP (nm)[a]
CeO_2	22.88	30	14.041	0.1653	0.5470
MnO_x/CeO_2	20.48	37	15.126	0.1961	0.5504

[a]Estimated from XRD studies. [b]Obtained from BJH studies.

much smaller than that of Ce^{4+} ions (0.097 nm).[39,40] If Mn ions replace Ce^{4+} ions in the CeO_2 lattice, a lattice contraction must be observed due to the smaller ionic radii of Mn ions with respect to Ce^{4+}. Interestingly, a lattice expansion in CeO_2 is found after the addition of MnO_x (Table 1). This observation indicates that no Mn ions are doped into the CeO_2 lattice. Several works reported that the conversion of Ce^{4+} to Ce^{3+} is a key reason for the expansion of the ceria lattice.[41−45] The radius of Ce^{3+} (0.114 nm) is higher than that of Ce^{4+} (0.097 nm); hence, there is an expansion in the ceria lattice during the reduction of Ce^{4+} to Ce^{3+}. The estimation of the relative strength of Ce^{3+} and Ce^{4+} in the CeO_2 and MnO_x/CeO_2 samples has been made using XPS (Figure 4A) and STEM-LEES studies (Figure 5C and D) and the results are presented in the following paragraphs.

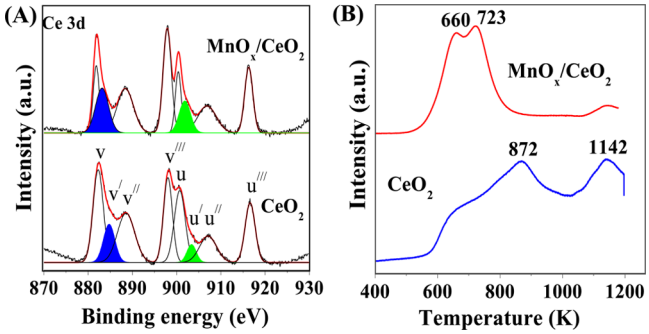

Figure 4. (A) Ce 3d XPS spectra and (B) H_2-TPR studies of the CeO_2 and MnO_x/CeO_2 samples.

The Raman spectra of CeO_2 nanocubes and MnO_x-dispersed CeO_2 nanocubes are shown in Figure 3B. A sharp Raman peak was observed at ~464 cm^{-1} for both samples, which indicates the presence of the Raman-active F_{2g} mode of fluorite-structured CeO_2 with the space group $Fm3m$.[46−48] This observation supports the XRD results (Figure 3A). Additionally, a broad peak was found at ~637 cm^{-1} for the MnO_x/CeO_2 sample, which can be assigned to α-Mn_2O_3.[37,49,50] The F_{2g} band of CeO_2 cubes is changed significantly after the addition of MnO_x (inset of Figure 3B). In particular, the F_{2g} band of the MnO_x/CeO_2 sample is shifted toward lower wavenumbers with respect to CeO_2 cubes. Variation in the Ce−O vibration frequencies is a key reason for this peak shift.[51−54] This fascinating observation reveals the existence of a strong interaction between MnO_x and CeO_2, enabling changes in the Ce−O bond. Generally, vibrations are slower for the expanded lattice; consequently, the F_{2g} band shifts to lower wavenumbers.[51] Therefore, the lattice expansion, as evidenced from XRD studies (Figure 3A and Table 1), is the main reason for the F_{2g} band shifting in the MnO_x/CeO_2 sample. The ceria-based samples usually show a Raman band in the range of ~580−600 cm^{-1}, corresponding to the presence of oxygen vacancy defects in CeO_2.[52−54] Remarkably, the MnO_x/CeO_2 sample exhibits a higher intensity band centered at ~581 cm^{-1}. This observation implies that the addition of MnO_x to the CeO_2 cubes results in the creation of abundant oxygen vacancies. It is a well-known fact that the amount of oxygen vacancies is directly related to the concentration of Ce^{3+} ions.[38] It is therefore expected that the MnO_x/CeO_2 sample may contain more Ce^{3+} ions compared with that of bare CeO_2 nanocubes, which was meticulously investigated with the help of XPS (Figure 4A) and STEM-EELS studies (Figure 5C and D).

The N_2 adsorption−desorption isotherms of the CeO_2 and MnO_x/CeO_2 samples can be classified as Type IV isotherms with H1-type hysteresis (Supporting Information, Figure S2). Data obtained from the BJH analysis indicates broad pore size distributions with average pore diameters of ~14.041 and 15.126 nm for CeO_2 and MnO_x/CeO_2 samples, respectively (Table 1 and Supporting Information, Figure S3). The pore volumes for CeO_2 and MnO_x/CeO_2 samples are found to be ~0.1653 and 0.1961 cm^3/g, respectively (Table 1). The estimated average ceria crystallite sizes are ~22.88 and 20.48 nm for CeO_2 and MnO_x/CeO_2 samples, respectively (Table 1). This observation reveals that the crystalline growth of CeO_2 is

DOI: 10.1021/acsami.5b03988
ACS Appl. Mater. Interfaces 2015, 7, 16525−16535

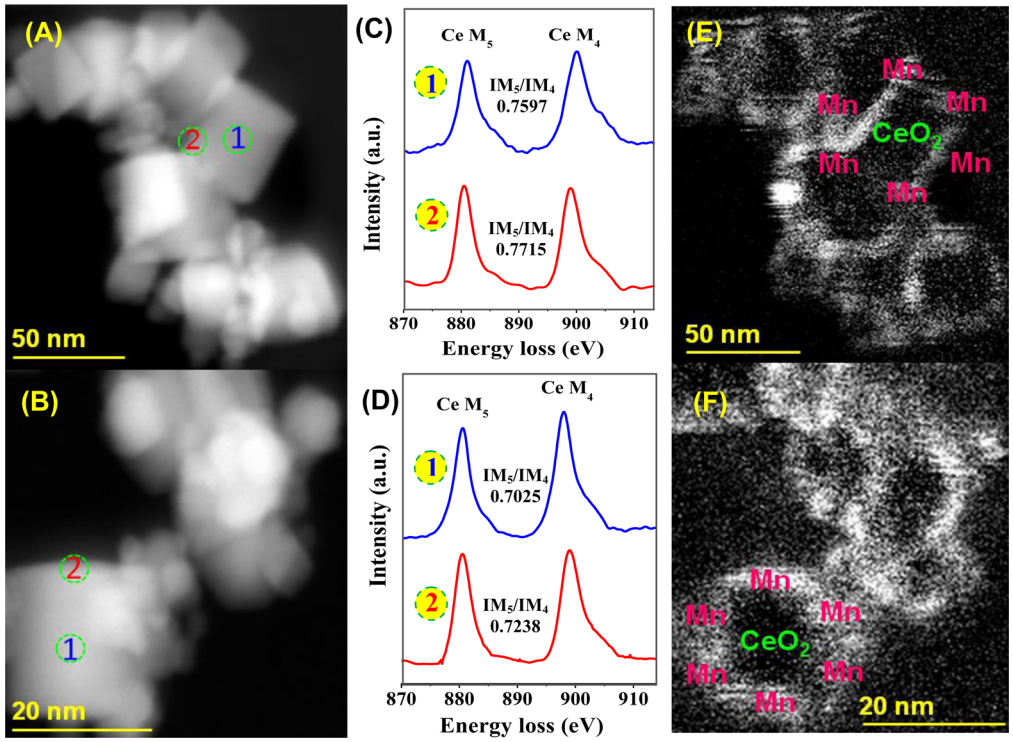

Figure 5. (A and B) HAADF-STEM images, (C and D) Ce $M_{5,4}$ EELS spectra recorded on the CeO_2 surface (1) and at the MnO_x/CeO_2 interface (2), and (E and F) STEM-EELS elemental mapping images of the MnO_x/CeO_2 heteronanostructures.

quite inhibited with the addition of MnO_x, and this may be due to interactions between MnO_x and CeO_2. The obtained BET surface area values for CeO_2 and MnO_x/CeO_2 samples are ~30 and 37 $m^2\ g^{-1}$, respectively, in line with the crystallite size of the samples (Table 1).

Figure 4A shows the Ce 3d XPS spectra of the CeO_2 and MnO_x/CeO_2 samples. As shown in the figure, the complex Ce 3d spectra of the samples are fitted with eight peaks.[55−57] The bands labeled with u' and v' represent the $3d^{10}4f^1$ electronic state of Ce^{3+}, and the peaks labeled by u, u'', u''', v, v'', and v''' indicate the $3d^{10}4f^0$ electronic state of Ce^{4+}. The appearance of all these peaks reveals that both Ce^{3+} and Ce^{4+} species exist in the synthesized samples. This result indicates the redox nature of the samples. The presence of Ce^{3+} ions could lead to a charge imbalance, creation of oxygen vacancies, and unsaturated chemical bonds in the CeO_2 lattice.[55] The relative strength of Ce^{3+} and Ce^{4+} in the CeO_2 and MnO_x/CeO_2 samples was estimated from the ratio of integrated Ce^{3+} peaks (u' and v') to the total Ce^{3+} (u' and v') and Ce^{4+} peaks (u, u'', u''', v, v'', and v''') as follows[57,58]

$$Ce^{3+}\text{concentration} = [A(Ce^{3+})]/[A(Ce^{3+}) + A(Ce^{4+})]$$

The concentration of Ce^{3+} ions in CeO_2 and MnO_x/CeO_2 samples was found to be ~0.1207 and 0.2191, respectively. It was clear that the MnO_x/CeO_2 sample exhibits a greater number of Ce^{3+} ions, indicating the highly reducible nature of the heteronanostructures. Therefore, the presence of a high concentration of Ce^{3+} ions in the MnO_x/CeO_2 sample is the reason for the unusual lattice expansion (Figure 3A and Table 1) and abundant oxygen vacancy defects (Figure 3B).

The obtained O 1s XP spectra of the samples show two peaks at ~529.15 and 531.74 eV, which can be assigned to O_2 ions in the CeO_2 or MnO_x lattice and adsorbed oxygen species, respectively (Supporting Information, Figure S4A).[59] The Mn 2p XPS spectrum of the MnO_x/CeO_2 sample shows two peaks centered at ~641.5 and 653.23 eV, corresponding to Mn $2p_{3/2}$ and Mn $2p_{1/2}$, respectively (Supporting Information, Figure S5).[60] The deconvolution of the Mn $2p_{3/2}$ peak indicates the presence of Mn^{3+} (~641.4 eV) and Mn^{4+} (~643.5 eV) species. Figure 4B shows the H_2-TPR studies of the samples. Pure CeO_2 nanocubes exhibit two reduction peaks centered at ~872 and ~1142 K, corresponding to surface and bulk reduction of cerium oxide, respectively.[61] The MnO_x/CeO_2 heteronanostructures exhibit two reduction peaks centered at ~660 and ~723 K. The low temperature peak reveals the reduction of Mn_2O_3 to Mn_3O_4, and the peak at high temperature indicates the combined reductions of Mn_3O_4 to MnO and surface Ce^{4+} to Ce^{3+} species.[62] It was clear from the reduction profiles of CeO_2 and MnO_x/CeO_2 samples that the addition of MnO_x to CeO_2 results in an improvement in the surface reduction of cerium oxide. This is beneficial from a catalysis point of view because any heterogeneous catalytic reaction inherently takes place on the catalyst surface.

The results obtained from XRD, Raman, and XPS studies reveal that the structural and redox properties of CeO_2 nanocubes are signficantly modified after the addition of MnO_x. Particularly, higher numbers of Ce^{3+} ions, abundant oxygen vacancy defects, and superior surface-reducible nature of cerium oxide were found for the MnO_x/CeO_2 heteronanostructures compared with those of CeO_2 nanocubes. All these attractive properties are directly related to each other. It can be expected that all these catalytically favorable properties are present at the interface of MnO_x and CeO_2. This prediction can be explained by the existence of a strong interaction between the MnO_x and CeO_2 phases at their interface. For this, STEM analysis coupled with HAADF and EELS has been performed, which is an efficient technique for understanding the atomic and electronic structure of materials with

DOI: 10.1021/acsami.5b03988
ACS Appl. Mater. Interfaces 2015, 7, 16525−16535

subnanometer spatial resolution. Panels A and B in Figure 5 show the HAADF-STEM images of the MnO_x/CeO_2 sample. Note that CeO_2 nanocubes are clearly observed in both images. In contrast, the presence of MnO_x species on the CeO_2 cubes is unclear from HAADF-STEM pictures. For this, STEM-EELS elemental mapping has been undertaken for both images (Figure 5E and F). Interestingly, the Mn species are well-dispersed along the edges of the CeO_2 cubes. This unusual decoration gives ambiguity (i.e., the reducible nature of cerium oxide is enhanced, whether on the surface of CeO_2 or at the MnO_x/CeO_2 interface). For this, Ce $M_{5,4}$ EELS analysis has been conducted on the CeO_2 surface (1) and at the MnO_x/CeO_2 interface (2) as shown in Figure 5C and D. It has been demonstrated that variations in the position of the Ce M_5 and Ce M_4 lines, the relative intensity ratio of these lines, and the appearance of shoulders at the right side of the peaks can be used as the fingerprint of redox properties of cerium oxide.[63−65] In particular, the relative intensity ratio of the Ce M_5 and Ce M_4 peaks (IM_5/IM_4) is used for understanding the redox nature of the ceria-based materials: a higher ratio indicates a higher reducible nature. The estimated IM_5/IM_4 values at different spots for MnO_x/CeO_2 sample are presented in Figure 5C and D. Interestingly, higher IM_5/IM_4 values were found at the MnO_x/CeO_2 interface with respect to the CeO_2 surface. These results confirm that the reducible nature of cerium oxide is greatly enhanced at the MnO_x/CeO_2 interface. The existence of strong interface interactions between MnO_x and CeO_2 is the reason for the enhanced reducible nature at the MnO_x/CeO_2 interface. The unusual lattice expansion (Figure 3A), abundant oxygen vacancy defects (Figure 3B), and higher number of Ce^{3+} ions (Figure 4A) in MnO_x/CeO_2 heteronanostructures can also be explained by strong interface interactions.

3.2. Catalytic Activity Studies. *3.2.1. Diesel Soot Oxidation.* Soot emitted from diesel engines exhibits massive environmental and human health problems, including lung cancer; thus, its removal is an urgent task.[35,51,66] The oxidation of soot using catalysts is a well-established industrial process to eliminate soot from diesel engines.[67] Particularly, catalytic soot oxidation at low temperatures is desirable to prevent damage to diesel engines against elevated thermal conditions. Figure 6 shows the catalytic performance of MnO_x/CeO_2 heteronanostructures for diesel soot oxidation. For comparison, soot oxidation without catalyst as well as using bare CeO_2 nanocubes has been studied. It was obvious from Figure 6A that the conversion of soot increases with increasing temperature. For a better comparison, the T_{50} values (the temperature at which 50% of soot conversion was achieved) of the samples are estimated (Figure 6B). The CeO_2 nanocubes have been found to exhibit a higher catalytic performance (T_{50} ~723 K) with an enormous temperature difference of 158 K with respect to uncatalyzed conditions (T_{50} ~881 K). This observation strongly highlights the significance of CeO_2 in the elimination of diesel soot. On the other hand, the catalytic efficiency of CeO_2 nanocubes was significantly improved after the addition of MnO_x (T_{50} ~660 K). The difference between T_{50} values of MnO_x/CeO_2 and CeO_2 samples was found to be 63 K, revealing the promoting role of MnO_x on the efficiency of CeO_2 nanocubes for the oxidation of soot. Additionally, 100% soot conversion was found at ~750 and 801 K for MnO_x/CeO_2 and CeO_2 samples, respectively.

3.2.2. Continuous-Flow Benzylamine Oxidation. The selective oxidation of amines to imines is an important functional group transformation in the chemical industry due

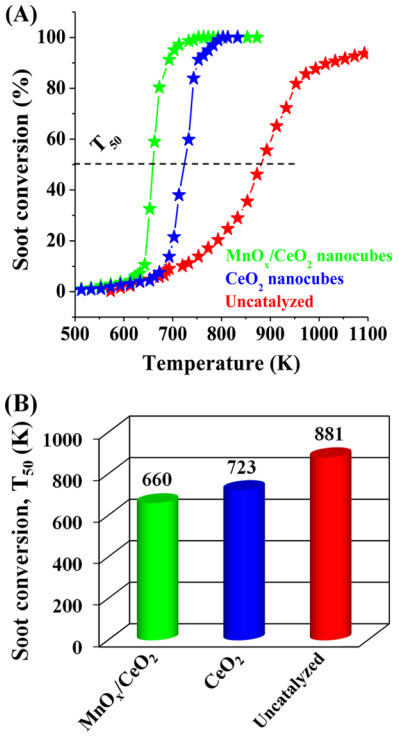

Figure 6. (A) Soot conversion (%) versus temperature (K) and (B) estimated T_{50} (K) values for CeO_2 nanocubes, MnO_x/CeO_2 heteronanostructures, and without catalyst conditions.

to the many useful applications of imines.[68−72] Imines are key building blocks for the production of fungicides, pharmaceuticals, fine chemicals, and heterocyclic drugs. A number of reports can be found in the literature for the oxidation of benzylamines over different homogeneous and heterogeneous catalysts under liquid phase conditions.[69,72] However, separation of the catalyst from the reaction mixture and its reusability are the crucial challenging issues under liquid-phase reaction conditions. Also, the use of hazardous solvents and stoichiometric oxidants is not an environmentally benign process. In contrast, performing the catalytic reactions under vapor-phase conditions (continuous-flow), a well-recognized industrial process, eliminates the problems related to catalyst separation and reusability. Hence, in this work, the oxidation of benzylamine was conducted under continuous-flow conditions. Molecular oxygen (O_2) is used as the oxidant because O_2 is a green and abundant oxidant and produces water as the only byproduct in the oxidation process.[68,73] Figure 7 shows the time-on-stream analysis of benzylamine oxidation over CeO_2 nanocubes and MnO_x/CeO_2 heteronanostructures. It was found that MnO_x/CeO_2 nanostructures show a higher catalytic performance compared with that of CeO_2 nanocubes. The conversion of benzylamine was found to be ~11.7 and 35.3% for CeO_2 and MnO_x/CeO_2 samples after 1 h of reaction time, respectively. Both CeO_2 and MnO_x/CeO_2 samples exhibit a noticeable steady performance in the oxidation of benzylamine with time. The achieved bezylamine conversions at 2, 3, 4, 5, 6, 7, and 8 h reaction times are found to be 39.4, 41.8, 42.1, 42.9, 44.1, 46.4, and 42.3% for the MnO_x/CeO_2 sample, respectively. Interestingly, the selectivity of dibenzylimine was drastically decreased from ~91 to 69% over the CeO_2 nanocubes after 1 h of reaction time. In contrast, there was no considerable variation in the dibenzylimine selectivity (~94−98%) over the

DOI: 10.1021/acsami.5b03988
ACS Appl. Mater. Interfaces 2015, 7, 16525−16535

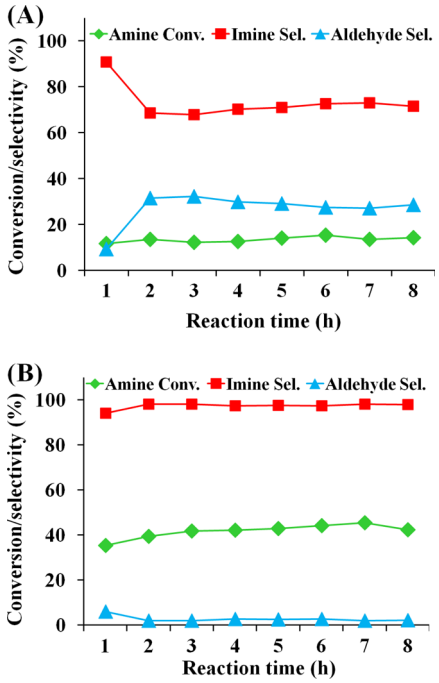

Figure 7. Continuous-flow benzylamine oxidation over (A) CeO_2 nanocubes and (B) MnO_x/CeO_2 heteronanostructures. Reaction conditions: O_2 flow rate 60 mL/h, catalyst amount (300 mg), benzylamine feed rate 0.5 mL/h, and reaction temperature (493 K).

MnO_x/CeO_2 heteronanostructures with reaction time. It is therefore concluded that the MnO_x/CeO_2 heteronanostructures selectively catalyze the oxidation of benzylamine to dibenzylimine.

3.2.3. Structure–Activity Relationships. The CeO_2 and MnO_x oxides are widely used candidates in several catalytic oxidation reactions due to the presence of multiple oxidation states of Ce (III and IV) and Mn (II, III, IV, and VII).[6−14] It has been reported that the reducible nature of ceria plays a beneficial role in the elimination of diesel soot.[21] Ceria is reduced by soot, resulting in the creation of oxygen vacancies at the soot/ceria interface during soot oxidation. Gas phase oxygen adsorbs onto the oxygen vacancies, enabling the generation of active oxygen species that contribute to the oxidation of soot by a spillover mechanism (Scheme 2).[51] It was found from XPS (Figure 4A) and H_2-TPR (Figure 4B) studies that CeO_2 nanocubes exhibit a considerable reducible

Scheme 2. Possible Mechanism for Soot Oxidation over MnO_x/CeO_2 Heteronanostructures

nature, hence showing higher soot oxidation efficiency with respect to uncatalyzed conditions (Figure 6). After the addition of MnO_x to CeO_2 nanocubes, their reducible nature is outstandingly improved (Figure 4), especially at the MnO_x/CeO_2 interface (Figure 5). As stated, ceria can be reduced by soot at the CeO_2/soot interface. Hence, the interfaces of MnO_x/CeO_2/soot may exhibit superior reducible nature and create large amounts of oxygen vacancies, explaining the exceptional performance of MnO_x/CeO_2 heteronanostructures for diesel soot oxidation at low temperatures (Figure 6 and Scheme 2).

Quite similar results were found for the oxidation of benzylamine as well (Figure 7). The efficiency of CeO_2 nanocubes in the oxidation of benzylamine was significantly improved after the addition of MnO_x. Most importantly, a high selectivity toward the dibenzylimine product (94−98%) was found for the MnO_x/CeO_2 sample at all reaction times. Two possible mechanisms are found in the literature for the oxidation of benzylamine to yield the dibenzylimine product (Scheme 3).[69,70] As shown in Scheme 3, an imine intermediate (PhCH═NH) is initially formed from the oxidative dehydrogenation of benzylamine in both pathways. Afterwards, hydrolysis of the imine intermediate by in situ generated water gives benzaldehyde, which readily couples with benzylamine to yield the dibenzylimine product (pathway A). Alternatively, the imine intermediate reacts with benzylamine to give the dibenzylimine product via the formation of a hemiaminal (pathway B). Catalytic results indicate the formation of benzaldehyde during the oxidation of benzylamine (Figure 7), confirming the formation of dibenzylimine via pathway A. Only trace amounts of benzaldehyde was found for the MnO_x/CeO_2 sample, suggesting that as soon as benzaldehyde is formed, it reacts instantly with benzylamine to give the dibenzylimine product. However, in the case of CeO_2 nanocubes, the dibenzylimine selectivity was drastically decreased after 1 h reaction time (Figure 7A). This result indicates that the CeO_2 nanocube catalyst has a low efficiency in the coupling reaction between the benzaldehyde and benzylamine to yield the final product (Scheme 3). As stated, the MnO_x/CeO_2 heteronanostructures exhibit an outstanding selectivity toward the dibenzylimine product at all reaction times, which is due to its high efficiency in the coupling reaction between benzaldehyde and benzylamine. It has been demonstrated that reduced CeO_2 plays a beneficial role in the selective oxidation and coupling reactions.[74,75] An enhancement in the ceria reducibility was found at the MnO_x/CeO_2 interface (Figure 5). Conversely, manganese oxides act as oxidizing agents due to the presence of mixed valences. When the particle size of a catalyst reduces to nanoscale range, an improvement in the catalyst efficiency can be found due to (quantum) size effects, higher density of the defects, and exposed low coordinated surface sites. The HRTEM and STEM-EELS studies demonstrate a high dispersion of MnO_x species along the edges of CeO_2 nanocubes with an average diameter of 9 ± 1 nm. Therefore, the observed catalytic performance of MnO_x/CeO_2 heteronanostructured catalyst in the oxidation of benzylamine is attributed to the superior reducible nature of cerium oxide and high dispersion of manganese oxide species. It is therefore suggested that the interface chemistry between the MnO_x nanoparticles and CeO_2 nanocubes plays a favorable role in modifying the structural and redox properties of the MnO_x/CeO_2 heteronanostrcutures, hence their catalytic performance.

DOI: 10.1021/acsami.5b03988
ACS Appl. Mater. Interfaces 2015, 7, 16525−16535

Scheme 3. Possible Reaction Pathways ((A) Hydrolysis of Intermediate and (B) Coupling of Intermediate and Benzylamine) for Continuous-Flow Benzylamine Oxidation over MnO_x/CeO_2 Heteronanostructures

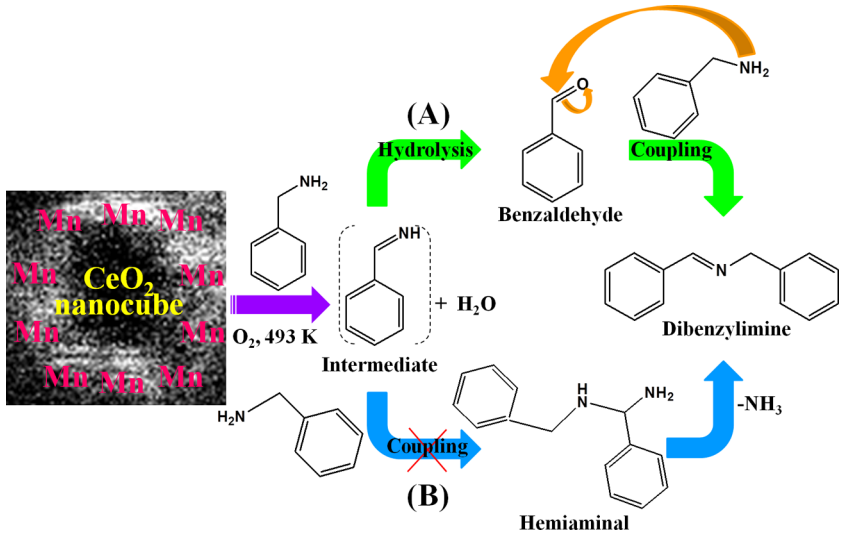

It is very important to study and correlate the physicochemical properties of materials before and after a catalytic reaction. This correlation provides necessary insight to beneficially modify key active parameters of a catalyst to improve its catalytic efficiency and durability in continuous-flow processes. Hence, the structural and morphological properties of the CeO_2 nanocubes and MnO_x/CeO_2 heteronanostructures were investigated after the benzylamine oxidation reaction. The recovered catalyst was washed with acetone multiple times to remove any adsorbed reactants and products, and then oven-dried at 523 K for 4 h. Figure 8 shows the HRTEM images of spent CeO_2 nanocubes and MnO_x/CeO_2 heteronanostructures. Different sized CeO_2 nanocubes can be observed with an average diameter of 19 ± 3 nm (Figure 8A and B). Furthermore, the particle size of MnO_x species is found to be ~10 ± 2 nm for the spent MnO_x/CeO_2 catalyst (Figure 8C and D). As estimated earlier, the particle size of CeO_2 and MnO_x are ~20 ± 2 and ~9 ± 1 nm, respectively, for the fresh CeO_2 nanocubes and MnO_x/CeO_2 heteronanostructures (Figures 1 and 2). These estimations indicate that there was not much variation in the particle size of MnO_x and CeO_2 after the reaction. However, it is interesting to note that the morphology of ceria is considerably changed for the spent CeO_2 cubes (Figure 8A and B) compared with the spent MnO_x/CeO_2 heteronanostructures (Figure 8C and D). This observation indicates the existence of a strong interaction between the MnO_x and CeO_2 components.

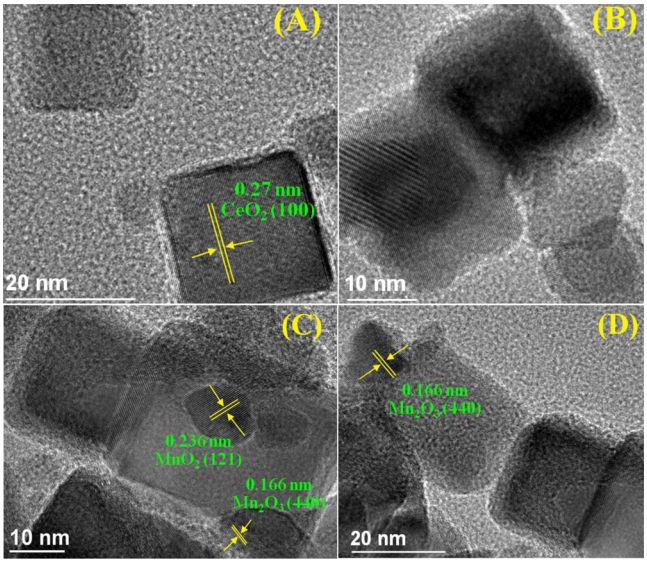

Figure 8. HRTEM images of the CeO_2 nanocubes (A and B) and MnO_x/CeO_2 heteronanostructures (C and D) after the benzylamine oxidation reaction.

Conversely, quite interesting results are found from the XPS studies. As observed in the O 1s XPS spectra of the fresh catalysts (Supporting Information, Figure S4A), two peaks at ~529.05 and 531.28 eV are also seen in the spectra of the spent catalysts. These peaks indicate the presence of O_2 ions in the CeO_2 or MnO_x lattice and adsorbed oxygen species, respectively (Supporting Information, Figure S4B). Interestingly, in addition to Mn^{3+} and Mn^{4+} species, Mn^{2+} is also found in the spent MnO_x/CeO_2 catalyst, whereas only Mn^{3+} and Mn^{4+} species are found in the fresh one (Supporting Information, Figure S5). This observation indicates that some proportion of Mn^{3+} and Mn^{4+} species are converted to Mn^{2+} during the benzylamine oxidation reaction. The Ce 3d XPS spectra of the spent catalysts show a total of eight peaks (u, u′, u″, u‴, v, v′, v″, and v‴), corresponding to the presence of both Ce^{3+} and Ce^{4+} ions (Supporting Information, Figure S6). Low concentrations of Ce^{3+} ions were found for the spent CeO_2 and MnO_x/CeO_2 samples (~0.1098 and 0.1956, respectively) compared with that of fresh CeO_2 and MnO_x/CeO_2 samples (~0.1207 and 0.2191, respectively). This observation indicates that the reducible properties of cerium oxide in the CeO_2 and MnO_x/CeO_2 samples are slightly decreased after the benzylamine oxidation reaction. CeO_2 is a well-known material for its superior oxygen storage and release properties.[7,8] Hence, it is possible that CeO_2 can absorb gas phase oxygen during the reaction. Consequently, the reducible properties of the cerium oxide can be influenced. Various diffraction peaks corresponding to fluorite-structured CeO_2 were noticed for spent CeO_2 and MnO_x/CeO_2 samples (Supporting Information, Figure S7). Interestingly, no XRD peaks related to an α-Mn_2O_3 phase were found for the spent

DOI: 10.1021/acsami.5b03988
ACS Appl. Mater. Interfaces 2015, 7, 16525−16535

MnO_x/CeO_2 sample. This might due to the lower amount of the Mn_2O_3 present in the spent sample because of the conversion of Mn^{3+} to Mn^{2+} during the reaction (XPS studies, Supporting Information, Figure S5). This thorough characterization of catalysts before and after the catalytic study could provide significant solutions for modifying key active parameters of the catalysts and, therefore, their catalytic efficiency and durability.

4. CONCLUSIONS

In this work, the structural characteristics and catalytic performance of CeO_2 nanocubes and MnO_x/CeO_2 heteronanostructures were evaluated for two important industrial applications, namely, diesel soot oxidation and continuous-flow benzylamine oxidation. The following conclusions can be drawn from the present study:

1. XRD and Raman measurements revealed an unusual lattice expansion in CeO_2 after the addition of MnO_x. This is due to the presence of more Ce^{3+} ions in the MnO_x/CeO_2 sample, as evidenced by XPS analysis.
2. HRTEM, HAADF-STEM, and STEM-EELS results indicate well-dispersed MnO_x species along the edges of the CeO_2 nanocubes, which forms a synergistic MnO_x/CeO_2 interface.
3. The detailed STEM-EELS investigation confirms the enhanced reducible nature of cerium oxide at the MnO_x/CeO_2 interface.
4. The MnO_x/CeO_2 heteronanostructures have been found to exhibit a remarkable catalytic performance toward both diesel soot oxidation and benzylamine oxidation compared to that of pure CeO_2 nanocubes.
5. Existence of a strong synergistic effect at the interface sites between CeO_2 and MnO_x in $MnOx/CeO_2$ heteronanostructures leads to catalytically favorable properties, hence its exceptional catalytic oxidation performance.
6. This systematic structure–activity correlation of MnO_x/CeO_2 heteronanostructured catalyst is believed to provide useful implications for designing multifunctional heteronanostructures with active interfaces and remarkable catalytic efficiency.

■ ASSOCIATED CONTENT

Supporting Information

TEM images, N_2-adsorption–desorption isotherms, pore size distribution profiles, O 1s XPS spectra, Mn 2p XPS spectrum, Ce 3d XPS and powder XRD profiles of the samples. The Supporting Information is available free of charge on the ACS Publications website at DOI: 10.1021/acsami.5b03988.

■ AUTHOR INFORMATION

Corresponding Author

*E-mail: suresh.bhargava@rmit.edu.au, Tel: +61 3 9925 2330.

Notes

The authors declare no competing financial interest.

■ ACKNOWLEDGMENTS

We thank Dr. Matthew Field, RMIT University for his immense help for technical assistance for characterizations. The authors duly acknowledge the RMIT Microscopy and Microanalysis Facility (RMMF) for providing access to instruments used in this study. We thank partial funding of this work from King Saud University, Deanship of Scientific Research via the Research Group Project (RGP-VPP-236) and Visiting Professor Program (VPP).

■ REFERENCES

(1) Jiang, H.-L.; Xu, Q. Recent Progress in Synergistic Catalysis over Heterometallic Nanoparticles. *J. Mater. Chem.* **2011**, *21*, 13705–13725.
(2) Han, M.; Liu, S.; Zhang, L.; Zhang, C.; Tu, W.; Dai, Z.; Bao, J. Synthesis of Octopus-Tentacle-Like Cu Nanowire-Ag Nanocrystals Heterostructures and Their Enhanced Electrocatalytic Performance for Oxygen Reduction Reaction. *ACS Appl. Mater. Interfaces* **2012**, *4*, 6654–6660.
(3) Wu, Z.; Xue, Y.; Wang, H.; Wu, Y.; Yu, H. ZnO Nanorods/Pt and ZnO Nanorods/Ag Heteronanostructure Arrays with Enhanced Photocatalytic Degradation of Dyes. *RSC Adv.* **2014**, *4*, 59009–59016.
(4) Li, S.-S.; Zheng, J.-N.; Wang, A.-J.; Tao, F.-L.; Feng, J.-J.; Chen, J.-R.; Yu, H. Branched Platinum-on-Palladium Bimetallic Heteronanostructures Supported on Reduced Graphene Oxide for Highly Efficient Oxygen Reduction Reaction. *J. Power Sources* **2014**, *272*, 1078–1085.
(5) Teng, X.; Han, W.; Wang, Q.; Li, L.; Frenkel, A. I.; Yang, J. C. Hybrid Pt/Au Nanowires: Synthesis and Electronic Structure. *J. Phys. Chem. C* **2008**, *112*, 14696–14701.
(6) Arena, F. Multipurpose Composite $MnCeO_x$ Catalysts for Environmental Applications. *Catal. Sci. Technol.* **2014**, *4*, 1890–1898.
(7) Sun, C.; Li, H.; Chen, L. Nanostructured Ceria-based Materials: Synthesis, Properties, and Applications. *Energy Environ. Sci.* **2012**, *5*, 8475–8505.
(8) Paier, J.; Penschke, C.; Sauer, J. Oxygen Defects and Surface Chemistry of Ceria: Quantum Chemical Studies Compared to Experiment. *Chem. Rev.* **2013**, *113*, 3949–3985.
(9) Chen, Z.; Jiao, Z.; Pan, D.; Li, Z.; Wu, M.; Shek, C.-H.; Wu, C. M. L.; Lai, J. K. L. Recent Advances in Manganese Oxide Nanocrystals: Fabrication, Characterization, and Microstructure. *Chem. Rev.* **2012**, *112*, 3833–3855.
(10) Chen, G.; Rosei, F.; Ma, D. Interfacial Reaction-Directed Synthesis of Ce–Mn Binary Oxide Nanotubes and Their Applications in CO Oxidation and Water Treatment. *Adv. Funct. Mater.* **2012**, *22*, 3914–3920.
(11) Wu, X.; Lin, F.; Xu, H.; Weng, D. Effects of Adsorbed and Gaseous NO_x Species on Catalytic Oxidation of Diesel Soot with MnO_x–CeO_2 Mixed Oxides. *Appl. Catal., B* **2010**, *96*, 101–109.
(12) Jampaiah, D.; Tur, K. M.; Venkataswamy, P.; Ippolito, S. J.; Sabri, Y. M.; Tardio, J.; Bhargava, S. K.; Reddy, B. M. Catalytic Oxidation and Adsorption of Elemental Mercury over Nanostructured CeO_2–MnO_x Catalyst. *RSC Adv.* **2015**, *5*, 30331–30341.
(13) Quiroz, J.; Giraudon, J.-M.; Gervasini, A.; Dujardin, C.; Lancelot, C.; Trentesaux, M.; Lamonier, J.-F. Total Oxidation of Formaldehyde over MnO_x-CeO_2 Catalysts: The Effect of Acid Treatment. *ACS Catal.* **2015**, *5*, 2260–2269.
(14) Xingyi, W.; Qian, K.; Dao, L. Catalytic Combustion of Chlorobenzene over MnO_x–CeO_2 Mixed Oxide Catalysts. *Appl. Catal., B* **2009**, *86*, 166–175.
(15) Kundu, P.; Anumol, E. A.; Nethravathi, C.; Ravishankar, N. Existing and Emerging Strategies for the Synthesis of Nanoscale Heterostructures. *Phys. Chem. Chem. Phys.* **2011**, *13*, 19256–19269.
(16) Zhang, D.; Du, X.; Shi, L.; Gao, R. Shape-Controlled Synthesis and Catalytic Application of Ceria Nanomaterials. *Dalton Trans.* **2012**, *41*, 14455–14475.
(17) Huang, W.; Gao, Y. Morphology-Dependent Surface Chemistry and Catalysis of CeO_2 Nanocrystals. *Catal. Sci. Technol.* **2014**, *4*, 3772–3784.
(18) Sreeremya, T. S.; Krishnan, A.; Remani, K. C.; Patil, K. R.; Brougham, D. F.; Ghosh, S. Shape Selective Oriented Cerium Oxide Nanocrystals Permit Assessment of the Effect of the Exposed Facets on Catalytic Activity and Oxygen Storage Capacity. *ACS Appl. Mater. Interfaces* **2015**, *7*, 8545–8555.

DOI: 10.1021/acsami.5b03988
ACS Appl. Mater. Interfaces 2015, 7, 16525–16535

(19) Sk, M. A.; Kozlov, S. M.; Lim, K. H.; Migani, A.; Neyman, K. M. Oxygen Vacancies in Self-Assemblies of Ceria Nanoparticles. *J. Mater. Chem. A* **2014**, *2*, 18329−18338.
(20) Maitarad, P.; Zhang, D.; Gao, R.; Shi, L.; Li, H.; Huang, L.; Rungrotmongkol, T.; Zhang, J. Combination of Experimental and Theoretical Investigations of $MnO_x/Ce_{0.9}Zr_{0.1}O_2$ Nanorods for Selective Catalytic Reduction of NO with Ammonia. *J. Phys. Chem. C* **2013**, *117*, 9999−10006.
(21) Aneggi, E.; Wiater, D.; de Leitenburg, C.; Llorca, J.; Trovarelli, A. Shape-Dependent Activity of Ceria in Soot Combustion. *ACS Catal.* **2014**, *4*, 172−181.
(22) Bhatta, U. M.; Reid, D.; Sakthivel, T.; Sayle, T. X. T.; Sayle, D.; Molinari, M.; Parker, S. C.; Ross, I. M.; Seal, S.; Möbus, G. Morphology and Surface Analysis of Pure and Doped Cuboidal Ceria Nanoparticles. *J. Phys. Chem. C* **2013**, *117*, 24561−24569.
(23) Chen, Y.; Lv, S.; Chen, C.; Qiu, C.; Fan, X.; Wang, Z. Controllable Synthesis of Ceria Nanoparticles with Uniform Reactive {100} Exposure Planes. *J. Phys. Chem. C* **2014**, *118*, 4437−4443.
(24) Wu, X.; Yu, H.; Weng, D.; Liu, S.; Fan, J. Synergistic Effect between MnO and CeO_2 in the Physical Mixture: Electronic Interaction and NO Oxidation Activity. *J. Rare Earths* **2013**, *31*, 1141−1147.
(25) Wang, J.; Dong, X.; Wang, Y.; Li, Y. Effect of the Calcination Temperature on the Performance of a $CeMoO_x$ Catalyst in the Selective Catalytic Reduction of NO_x with Ammonia. *Catal. Today* **2015**, *245*, 10−15.
(26) Qi, G.; Li, W. *Catal. Today* **2015**; DOI: 10.1016/j.cattod.2015.03.020
(27) Li, H.; Wu, C.-Y.; Li, Y.; Li, L.; Zhao, Y.; Zhang, J. Role of Flue Gas Components in Mercury Oxidation over TiO_2 Supported MnO_x-CeO_2 Mixed-Oxide at Low Temperature. *J. Hazard. Mater.* **2012**, *243*, 117−123.
(28) Zhou, G.; Shah, P. R.; Gorte, R. J. A Study of Cerium−Manganese Mixed Oxides for Oxidation Catalysis. *Catal. Lett.* **2008**, *120*, 191−197.
(29) Zhang, Z.-C.; Xu, B.; Wang, X. Engineering Nanointerfaces for Nanocatalysis. *Chem. Soc. Rev.* **2014**, *43*, 7870−7886.
(30) Wu, Q.; Zhang, F.; Xiao, P.; Tao, H.; Wang, X.; Hu, Z.; Lu, Y. Great Influence of Anions for Controllable Synthesis of CeO_2 Nanostructures: From Nanorods to Nanocubes. *J. Phys. Chem. C* **2008**, *112*, 17076−17080.
(31) Yang, S.; Gao, L. Controlled Synthesis and Self-Assembly of CeO_2 Nanocubes. *J. Am. Chem. Soc.* **2006**, *128*, 9330−9331.
(32) Deori, K.; Kalita, C.; Deka, S. (100) Surface-Exposed CeO_2 Nanocubes as an Efficient Heterogeneous Catalyst in the Tandem Oxidation of Benzyl Alcohol, para-Chlorobenzyl Alcohol and Toluene to the Corresponding Aldehydes Selectively. *J. Mater. Chem. A* **2015**, *3*, 6909−6920.
(33) Javed, Q.; Wang, F. P.; Rafique, M. Y.; Toufiq, A. M.; Li, Q. S.; Mahmood, H.; Khan, W. Diameter-Controlled Synthesis of α-Mn_2O_3 Nanorods and Nanowires with Enhanced Surface Morphology and Optical Properties. *Nanotechnology* **2012**, *23*, 415603−415610.
(34) Lin, Y.-G.; Chen, Y.-C.; Miller, J. T.; Chen, L.-C.; Chen, K.-H.; Hsu, Y.-K. Hierarchically Porous Calcium-containing Manganese Dioxide Nanorod Bundles with Superior Photoelectrochemical Activity. *ChemCatChem* **2014**, *6*, 1684−1690.
(35) Sudarsanam, P.; Kuntaiah, K.; Reddy, B. M. Promising Ceria−Samaria-Based Nano-Oxides for Low Temperature Soot Oxidation: A Combined Study of Structure−Activity Properties. *New J. Chem.* **2014**, *38*, 5991−6001.
(36) Sudarsanam, P.; Mallesham, B.; Durgasri, D. N.; Reddy, B. M. Physicochemical Characterization and Catalytic CO Oxidation Performance of Nanocrystalline Ce−Fe Mixed Oxides. *RSC Adv.* **2014**, *4*, 11322−11330.
(37) Luo, Y.; Deng, Y.-Q.; Mao, W.; Yang, X.-J.; Zhu, K.; Xu, J.; Han, Y.-F. Probing the Surface Structure of α-Mn_2O_3 Nanocrystals during CO Oxidation by Operando Raman Spectroscopy. *J. Phys. Chem. C* **2012**, *116*, 20975−20981.
(38) Sudarsanam, P.; Mallesham, B.; Reddy, P. S.; Großmann, D.; Grünert, W.; Reddy, B. M. Nano-Au/CeO_2 Catalysts for CO Oxidation: Influence of Dopants (Fe, La and Zr) on the Physicochemical Properties and Catalytic Activity. *Appl. Catal., B* **2014**, *144*, 900−908.
(39) Murugan, B.; Ramaswamy, A. V.; Srinivas, D.; Gopinath, C. S.; Ramaswamy, V. Nature of Manganese Species in $Ce_{1-x}Mn_xO_{2-\delta}$ Solid Solutions Synthesized by the Solution Combustion Route. *Chem. Mater.* **2005**, *17*, 3983−3993.
(40) Yu, X.; Li, J.; Wei, Y.; Zhao, Z.; Liu, J.; Jin, B.; Duan, A.; Jiang, G. Three-Dimensionally Ordered Macroporous $Mn_xCe_{1-x}O_\delta$ and Pt/$Mn_{0.5}Ce_{0.5}O_\delta$ Catalysts: Synthesis and Catalytic Performance for Soot Oxidation. *Ind. Eng. Chem. Res.* **2014**, *53*, 9653−9664.
(41) Marrocchelli, D.; Bishop, S. R.; Kilner, J. Chemical Expansion and its Dependence on the Host Cation Radius. *J. Mater. Chem. A* **2013**, *1*, 7673−7680.
(42) Migani, A.; Vayssilov, G. N.; Bromley, S. T.; Illas, F.; Neyman, K. M. Dramatic Reduction of the Oxygen Vacancy Formation Energy in Ceria Particles: a Possible Key to their Remarkable Reactivity at the Nanoscale. *J. Mater. Chem.* **2010**, *20*, 10535−10546.
(43) Vecchietti, J.; Bonivardi, A.; Xu, W.; Stacchiola, D.; Delgado, J. J.; Calatayud, M.; Collins, S. E. Understanding the Role of Oxygen Vacancies in the Water Gas Shift Reaction on Ceria-Supported Platinum Catalysts. *ACS Catal.* **2014**, *4*, 2088−2096.
(44) Chen, L.; Fleming, P.; Morris, V.; Holmes, J. D.; Morris, M. A. Size-Related Lattice Parameter Changes and Surface Defects in Ceria Nanocrystals. *J. Phys. Chem. C* **2010**, *114*, 12909−12919.
(45) Lee, Y.; He, G.; Akey, A. J.; Si, R.; Flytzani-Stephanopoulos, M.; Herman, I. P. Raman Analysis of Mode Softening in Nanoparticle $CeO_{2-\delta}$ and Au-$CeO_{2-\delta}$ during CO Oxidation. *J. Am. Chem. Soc.* **2011**, *133*, 12952−12955.
(46) Taniguchi, T.; Sonoda, Y.; Echikawa, M.; Watanabe, Y.; Hatakeyama, K.; Ida, S.; Koinuma, M.; Matsumoto, Y. Intense Photoluminescence from Ceria-Based Nanoscale Lamellar Hybrid. *ACS Appl. Mater. Interfaces* **2012**, *4*, 1010−1015.
(47) Artiglia, L.; Agnoli, S.; Paganini, M. C.; Cattelan, M.; Granozzi, G. TiO_2@CeO_x Core−Shell Nanoparticles as Artificial Enzymes with Peroxidase-Like Activity. *ACS Appl. Mater. Interfaces* **2014**, *6*, 20130−20136.
(48) Du, X.; Zhang, D.; Shi, L.; Gao, R.; Zhang, J. Morphology Dependence of Catalytic Properties of Ni/CeO_2 Nanostructures for Carbon Dioxide Reforming of Methane. *J. Phys. Chem. C* **2012**, *116*, 10009−10016.
(49) Cao, H.; Wu, X.; Wang, G.; Yin, J.; Yin, G.; Zhang, F.; Liu, J. Biomineralization Strategy to α-Mn_2O_3 Hierarchical Nanostructures. *J. Phys. Chem. C* **2012**, *116*, 21109−21115.
(50) Luo, Y.; Deng, Y.-Q.; Mao, W.; Yang, X.-J.; Zhu, K.; Xu, J.; Han, Y.-F. Probing the Surface Structure of α-Mn_2O_3 Nanocrystals during CO Oxidation by Operando Raman Spectroscopy. *J. Phys. Chem. C* **2012**, *116*, 20975−20981.
(51) Katta, L.; Sudarsanam, P.; Thrimurthulu, G.; Reddy, B. M. Doped Nanosized Ceria Solid Solutions for Low Temperature Soot Oxidation: Zirconium versus Lanthanum Promoters. *Appl. Catal., B* **2010**, *101*, 101−108.
(52) Ahn, K.; Yoo, D. S.; Prasad, D. H.; Lee, H.-W.; Chung, Y.-C.; Lee, J.-H. Role of Multivalent Pr in the Formation and Migration of Oxygen Vacancy in Pr-Doped Ceria: Experimental and First-Principles Investigations. *Chem. Mater.* **2012**, *24*, 4261−4267.
(53) Guo, M.; Lu, J.; Wu, Y.; Wang, Y.; Luo, M. UV and Visible Raman Studies of Oxygen Vacancies in Rare-Earth-Doped Ceria. *Langmuir* **2011**, *27*, 3872−3877.
(54) Kuntaiah, K.; Sudarsanam, P.; Reddy, B. M.; Vinu, A. Nanocrystalline Ce_{1-x} $Sm_xO_{2-\delta}$ (x= 0.4) Solid Solutions: Structural Characterization versus CO Oxidation. *RSC Adv.* **2013**, *3*, 7953−7962.
(55) He, C.; Shen, B.; Chen, J.; Cai, J. Adsorption and Oxidation of Elemental Mercury over Ce-MnO_x/TiPILCs. *Environ. Sci. Technol.* **2014**, *48*, 7891−7898.
(56) Paunovic, N.; Dohcevic-Mitrovic, Z.; Scurtu, R.; Askrabic, S.; Prekajski, M.; Matovic, B.; Popovic, Z. V. Suppression of Inherent

Ferromagnetism in Pr-Doped CeO_2 Nanocrystals. *Nanoscale* **2012**, *4*, 5469−5476.
(57) Liu, Z.; Zhu, J.; Li, J.; Ma, L.; Woo, S. I. Novel Mn−Ce−Ti Mixed-Oxide Catalyst for the Selective Catalytic Reduction of NO_x with NH_3. *ACS Appl. Mater. Interfaces* **2014**, *6*, 14500−14508.
(58) Maitarad, P.; Han, J.; Zhang, D.; Shi, L.; Namuangruk, S.; Rungrotmongkol, T. Structure−Activity Relationships of NiO on CeO_2 Nanorods for the Selective Catalytic Reduction of NO with NH_3: Experimental and DFT Studies. *J. Phys. Chem. C* **2014**, *118*, 9612−9620.
(59) Patil, N. S.; Uphade, B. S.; Jana, P.; Bhargava, S. K.; Choudhary, V. R. Epoxidation of Styrene by t-Butyl Hydroperoxide over Gold Supported on Yb_2O_3 and Other Rare Earth Oxides. *Chem. Lett.* **2004**, *33*, 400−401.
(60) Zhang, Y.; Qin, Z.; Wang, G.; Zhu, H.; Dong, M.; Li, S.; Wu, Z.; Li, Z.; Wu, Z.; Zhang, J.; Hu, T.; Fan, W.; Wang, J. Catalytic Performance of MnO_x−NiO Composite Oxide in Lean Methane Combustion at Low Temperature. *Appl. Catal., B* **2013**, *129*, 172−181.
(61) Alhumaimess, M.; Lin, Z.; Weng, W.; Dimitratos, N.; Dummer, N. F.; Taylor, S. H.; Bartley, J. K.; Kiely, C. J.; Hutchings, G. J. Oxidation of Benzyl Alcohol by using Gold Nanoparticles Supported on Ceria Foam. *ChemSusChem* **2012**, *5*, 125−131.
(62) Gao, R.; Zhang, D.; Maitarad, P.; Shi, L.; Rungrotmongkol, T.; Li, H.; Zhang, J.; Cao, W. Morphology-Dependent Properties of MnO_x/ZrO_2−CeO_2 Nanostructures for the Selective Catalytic Reduction of NO with NH_3. *J. Phys. Chem. C* **2013**, *117*, 10502−10511.
(63) Gonzalez-Rovira, L.; Sanchez-Amaya, J. M.; Lopez-Haro, M.; del Rio, E.; Hungr1a, A. B.; Midgley, P.; Calvino, J. J.; Bernal, S.; Botana, F. J. Single-Step Process to Prepare CeO_2 Nanotubes with Improved Catalytic Activity. *Nano Lett.* **2009**, *9*, 1395−1400.
(64) Li, Z.-P.; Toshiyuki, M.; Auchterlonie, G. J.; Zou, J.; John, D. Mutual Diffusion Occurring at the Interface between $La_{0.6}Sr_{0.4}Co_{0.8}Fe_{0.2}O_3$ Cathode and Gd-doped Ceria Electrolyte during IT-SOFC Cell Preparation. *ACS Appl. Mater. Interfaces* **2011**, *3*, 2772−2778.
(65) Rovira, L. G.; Delgado, J. J.; ElAmrani, K.; del Rio, E.; Chen, X.; Calvino, J. J.; Botana, F. J. Synthesis of Ceria-Praseodimia Nanotubes with High Catalytic Activity for CO Oxidation. *Catal. Today* **2012**, *180*, 167−173.
(66) Frank, B.; Schlögl, R.; Su, D. S. Diesel Soot Toxification. *Environ. Sci. Technol.* **2013**, *47*, 3026−3027.
(67) Sudarsanam, P.; Hillary, B.; Deepa, D. K.; Amin, M. H.; Mallesham, B.; Reddy, B. M.; Bhargava, S. K. Highly Efficient Cerium Dioxide Nanocubes-Based Catalyst for Low Temperature Diesel Soot Oxidation: Cooperative Effect of Cerium- and Cobalt-Oxides. *Catal. Sci. Technol.* **2015**, *5*, 3496−3500.
(68) Sudarsanam, P.; Rangaswamy, A.; Reddy, B. M. An Efficient Noble Metal-Free Ce−Sm/SiO_2 Nanooxide Catalyst for Oxidation of Benzylamines under Ecofriendly Conditions. *RSC Adv.* **2014**, *4*, 46378−46382.
(69) Schümperli, M. T.; Hammond, C.; Hermans, I. Developments in the Aerobic Oxidation of Amines. *ACS Catal.* **2012**, *2*, 1108−1117.
(70) Hammond, C.; Schümperli, M. T.; Hermans, I. Insights into the Oxidative Dehydrogenation of Amines with Nanoparticulate Iridium Oxide. *Chem. - Eur. J.* **2013**, *19*, 13193−13198.
(71) Dimitratos, N.; Lopez-Sanchez, J. A.; Hutchings, G. J. Selective Liquid Phase Oxidation with Supported Metal Nanoparticles. *Chem. Sci.* **2012**, *3*, 20−44.
(72) Largeron, M. Protocols for the Catalytic Oxidation of Primary Amines to Imines. *Eur. J. Org. Chem.* **2013**, *2013*, 5225−5235.
(73) Sudarsanam, P.; Mallesham, B.; Durgasri, N. D.; Reddy, B. M. Physicochemical and Catalytic Properties of Nanosized Au/CeO_2 Catalysts for Eco-friendly Oxidation of Benzyl Alcohol. *J. Ind. Eng. Chem.* **2014**, *20*, 3115−3121.
(74) Vivier, L.; Duprez, D. Ceria-Based Solid Catalysts for Organic Chemistry. *ChemSusChem* **2010**, *3*, 654−678.
(75) Selvamani, A.; Selvaraj, M.; Krishnan, P. S.; Gurulakshmi, M.; Shanthi, K. Low Temperature Vapor Phase Selective Oxidation of Ethylbenzene over $Ce_{1-x}Mn_xO_2$ Nanocubes. *Appl. Catal., A* **2015**, *495*, 92−103.

DOI: 10.1021/acsami.5b03988
ACS Appl. Mater. Interfaces 2015, 7, 16525−16535